

High-pressure structural evolution of undoped tetragonal nanocrystalline zirconia

P. Bouvier,* E. Djurado, and G. Lucazeau†

Laboratoire d'Electrochimie et de Physicochimie des Matériaux et des Interfaces, INPG-CNRS, 1130 rue de la piscine, BP 75, Domaine Universitaire, 38402 Saint Martin d'Hères Cedex, France

T. Le Bihan

ESRF, BP 220, 38043 Grenoble Cedex, France

(Received 2 March 2000)

The structure of nanocrystallized zirconia has been investigated in the 1–40-GPa pressure range at ambient temperature. A continuous transformation towards the ideal fluorite cubic structure is observed from 8 GPa. The complete transformation seems to be achieved at 30 GPa. The compressibility of the tetragonal and cubic forms are derived and discussed.

I. INTRODUCTION

Zirconia (ZrO_2) exhibits various structural polymorphs. Below its melting point (2800 K), at atmospheric pressure, ZrO_2 crystallizes in a cubic fluorite type structure (O_h^5 , $Fm\bar{3}m$, $Z=1$).¹ When temperature is decreased at atmospheric pressure two structural transitions are observed. The first one takes place at 2640 K and corresponds to the cubic-tetragonal (D_{4h}^{15} , $P4_2/nmc$, $Z=2$) (Refs. 2 and 3) second-order transition. The second one is of martensitic type and generates the room-temperature stable monoclinic form (C_{2h}^5 , $P2_1/c$, $Z=4$) (Refs. 4–6) below 1440 K.

Several high-pressure orthorhombic forms have also been evidenced. The first orthorhombic structure O_I ($Pbca$, $Z=4$) (Refs. 7–9) exists in the 3–22-GPa applied pressure range at ambient temperature depending upon zirconia grain size and sample history. At 22 GPa, another orthorhombic structure O_{II} is observed ($Pnam$, $Z=4$, cotunnite $PbCl_2$ type)^{10–12} which can be retained at room conditions by decompression. High-pressure and high-temperature quenched structures of zirconia have also been evidenced using x rays or neutron diffraction and two other orthorhombic structures named O_{III} and O_{IV} have been suspected below 50 GPa and 1200 K.^{13–18} Figure 1 sketches a pressure-temperature phase diagram based on that given in Ref. 11 where the existence domain for these possible orthorhombic forms has not been represented.

The introduction of trivalent dopants, with associated oxygen vacancies or the addition of either oversized or undersized tetravalent dopants into ZrO_2 , is known to stabilize at room temperature different metastable zirconia polymorphs such as the above-mentioned tetragonal and cubic forms. Undoped tetragonal zirconia can also be stabilized at ambient temperature by a crystallite size effect. Moreover, recent Raman characterization performed on zirconia thin films grown during zircaloy oxidation demonstrates that a tetragonal zirconia is stabilized at the metal-oxide interface at rather low temperature (630 K), by high compressive stresses (≥ 2 GPa).¹⁹ Thus the precise knowledge of the P - T phase diagram of zirconia and the influence of structural defects, such as disorder or grain size, on the phases boundaries, is of

particular interest when trying to understand the corrosion process of zircaloy substrates.

Recently, room-temperature undoped tetragonal nanocrystallized zirconia (NZ) has been characterized by Raman spectrometry under high pressure.²⁰ This compound exhibits a continuous transformation toward a fluorite-type structure. The Raman spectrometry is known to give structural information on a short-range scale typically comprised between 10 and 50 Å and for this reason it was fundamental to check that this transformation is observable on a long-range scale.

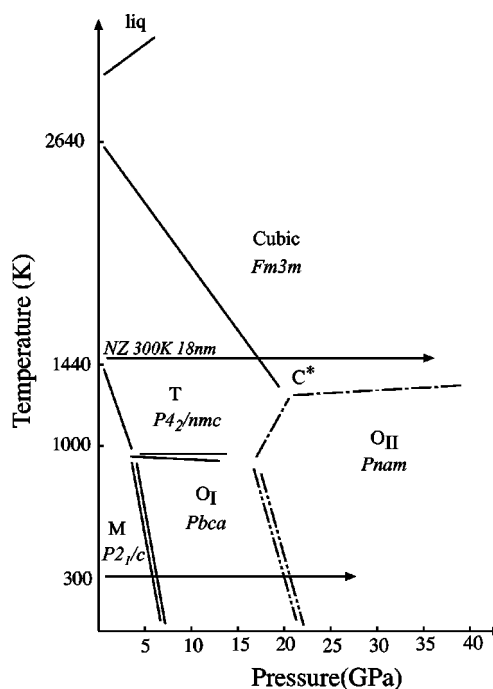


FIG. 1. Revisited pressure-temperature phase diagram of zirconia. Plain lines correspond to Refs. 3, 6, and 7. Dashed dot line corresponds to Refs. 7 and 15. Dashed double dot lines correspond to Refs. 14 and 15. The C^* corresponds to the hypothetical new phase presented in Ref. 13. The lower arrow corresponds to experimental excursion performed using Raman spectrometry on pure monoclinic zirconia. The higher arrow corresponds to the present high-pressure excursion for room-temperature NZ.

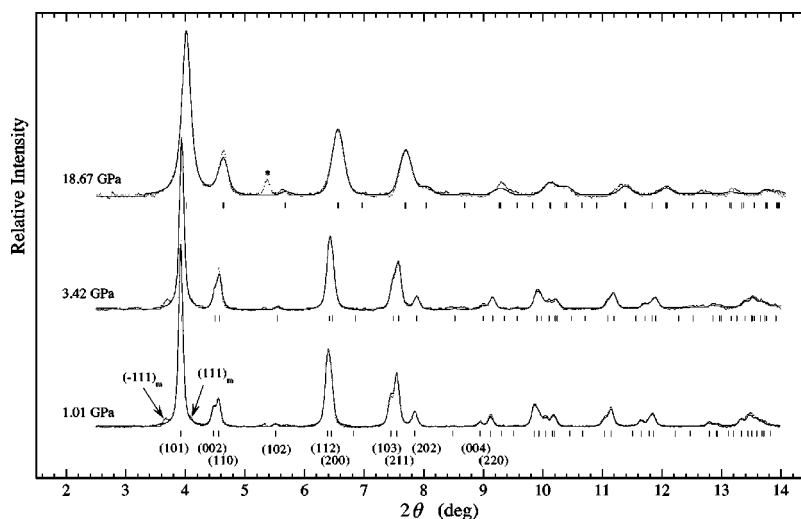


FIG. 2. Experimental x-ray diffractograms measured in cell 1 in the 1–20-GPa pressure range. The calculated diagram (solid line) in tetragonal $P4_2/nmc$ space group is also presented along with the corresponding indices. The asterisk corresponds to the stainless steel chamber.

Moreover, when considering the generalized P - T phase diagram of zirconia given in Ref. 11 and starting from a tetragonal zirconia stabilized at room temperature by a size effect, two different structural transformations can be expected with pressure increase: A tetragonal $\rightarrow O_{IV} \rightarrow O_{II}$ or a tetragonal \rightarrow cubic phase transition.

The present work is focused on the structure determination of nanocrystalline tetragonal undoped zirconia in the 1–40 GPa pressure range by hydrostatic high-pressure x-ray diffraction (XRD). Structural parameters extracted from Rietveld refinements are presented and discussed in order to evidence the structure of the zirconia high-pressure form. In the last part, the determination of compressibility is presented.

II. EXPERIMENTAL AND DATA ANALYSIS

Undoped tetragonal zirconia has been prepared by spray pyrolysis using an ultrasonic atomizer.²¹ This technique allows to obtain nanocrystallized material and thus to stabilize the tetragonal structure at room temperature. As previously determined,²² the average crystallite size was found close to 18 nm using Debye-Scherrer formula. Monoclinic zirconia content was found below 1 wt % from Raman spectrometry and XRD quantitative measurements.

Hydrostatic high-pressure XRD experiments have been performed at room temperature using the ID30 beamline of the European Synchrotron Radiation Facility (ESRF, Grenoble, France). Diffraction patterns have been collected using an image plate detector located 450 mm from the pressure cell chamber in an angle dispersive geometry. Exposure time of 300 s and two tilts of the cell at $\pm 6.5^\circ$ have been selected to get the best signal/noise ratio and enlarge the angular collection. The two dimensional diffraction patterns have been integrated over θ using FIT2D software.

Two XRD experiments have been performed successively. One in the 1–20-GPa pressure range using the Raman high-pressure diamond-anvil cell working with an ethanol-methanol-water mixture as pressure transmitting medium. This cell is characterized by a limited angle of collection

(15°) and imposed the use of short wavelength ($\lambda = 0.2022 \text{ \AA}$). The second experiment has been performed in the 20–40-GPa pressure range using cell with larger collection aperture and specially designed for XRD studies. The pressure transmitting medium was nitrogen and the incident wavelength $\lambda = 0.3066 \text{ \AA}$ has been selected in order to increase the angular resolution of 002 and 110 doublet. The pressure has been measured using the shift of R_1 and R_2 ruby fluorescence lines.²³ The two cells will be referred to as cell 1 and cell 2, respectively, for the 1–20 and 20–40-GPa pressure ranges.

Twenty diffractograms have been recorded in the 1–40-GPa range. Rietveld analyses of the data have been carried out using FULLPROF software.²⁴ The $P4_2/nmc$ and $Fm3m$ space groups have been systematically probed. The parameters refined are the scale factor, the lattice parameters (a and c), the oxygen positional parameter (δ shift from ideal cubic position), and the isotropic thermal parameters for both zirconium and oxygen ions. The peak shape is described by a pseudo-Voigt function. The profile parameters u, v, w and the mixing parameter of the pseudo-Voigt function have been refined in a first step and were found close to the nominal values for the resolution function of the instrument. In order to further reduce the number of free parameters, the background was obtained by interpolation between selected points and was kept fixed.

III. RESULTS

Figures 2 and 3 present some diffractograms of NZ in the two pressure ranges investigated in cells 1 and 2, respectively. At 1 and 3.4 GPa, the weak features located at $2\theta \approx 3.5$ and 4° are attributed to $\bar{1}11$ and 111 diffraction lines of traces of monoclinic zirconia. The main difference between 1 and 18-GPa diagrams is the position of the diffraction peaks and the collapsing of doublets splitting such as for example those at $2\theta \approx 4.5, 7.5,$ and 9° . The peak marked with an asterisk is unambiguously attributed to the stainless steel chamber. For pressure between 3 and 15 GPa, introduc-

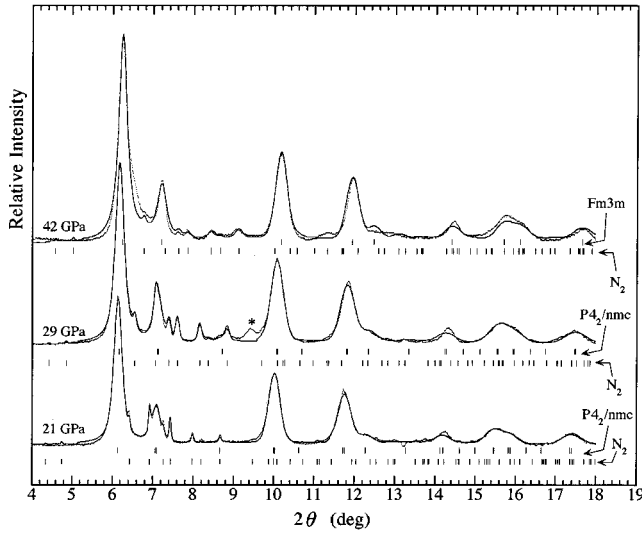


FIG. 3. Experimental x-ray diffractograms measured in cell 2 in the 20–40-GPa pressure range. The calculated diagram (solid line) in tetragonal $P4_2/nmc$ and cubic $Fm\bar{3}m$ space groups are presented along with the corresponding indices. The ϵ phase ($R\bar{3}c$) of nitrogen transmitting medium were also introduced in the refinement. The asterisk corresponds to the stainless steel chamber.

tion of a preferential orientation was necessary to account for the large intensity of 110 diffraction peaks. This phenomenon is often observed when working with powders at high pressure.

The diffraction lines expected in both tetragonal and cubic structures have been reported in the figures along with their indices. In Fig. 3 the sharp lines corresponding to the ϵ phase ($R\bar{3}c$) of nitrogen used as pressure transmitting medium were introduced in the refinement. The obtained nitrogen molecular volume are in good agreement with the pressure-

volume curve determined by Olijnyk.²⁵ At 42 GPa, the diffractogram is close to the one expected for a fluorite structure. The line located at $2\theta \approx 7^\circ$ is too narrow to be reproduced by a 002 and 110 tetragonal doublet.

IV. DISCUSSION

A. Structural analysis and evidence of a transformation toward a cubic structure

The crystallographic structure of NZ at atmospheric pressure is nicely refined using tetragonal $P4_2/nmc$ space group. For some selected pressures, the refined parameters are listed in Table I together with corresponding reliability factors R_{Bragg} and χ^2 . The lattice parameters and the cell volume dependence with pressure are presented in Fig. 4 and 5, respectively. For $P=8$ GPa, the anisotropic ratio $c/a\sqrt{2}$ (Fig. 4) presents a discontinuity due to the fact that c and $a\sqrt{2}$ tend to become equal. A small discontinuity is also observed in the cell volume pressure dependence at this pressure. A similar anomaly has been previously detected from the frequency evolution of the Raman lines in the same pressure range (see Ref. 20). This pressure is slightly lower than the solidification pressure of alcohol mixture [$P=13$ GPa (Ref. 26)] and it is unlikely that observed structural changes mentioned above could be associated with such solidification.

Nevertheless, this anomaly cannot be considered as a clear signature of a phase transition. Actually, the 102 line which is observed up to 29 GPa is a proof that the structure is not already cubic at 8 GPa. The oxygen position are still shifted from their ideal cubic position, for instance $\delta=0.07$ for 10 GPa (see Table I). Moreover, up to 8 GPa, the δ parameter increases slightly while the anisotropic ratio decreases down to unity. This observation cannot satisfy the relationship proposed by Howard, Hunter, and Kim for sta-

TABLE I. Comparison of refined structural parameters for two possible structures at high pressure. B_{iso} are the isotropic Debye-Waller factors. $R_{\text{bragg}} = [\sum (y_{\text{obs}} - y_{\text{calc}})^2 / \sum (y_{\text{obs}})^2]^{1/2}$ and $\chi^2 = [\sum (y_{\text{obs}} - y_{\text{calc}})^2 / (N - P + C)]^{1/2}$ with N the total number of points, P the number of refined parameters, and C the number of constraints.

Pressure (GPa)	1	10.9	21.4	28.9	33.8	37.3			
Space group		$P4_2/nmc$		$Fm\bar{3}m$	$P4_2/nmc$	$Fm\bar{3}m$	$P4_2/nmc$	$Fm\bar{3}m$	$P4_2/nmc$
Lattice parameters									
a (Å)	3.5948(2)	3.565(2)	3.512(3)		3.495(1)		3.484(1)		3.478(2)
c (Å)	5.1824(7)	5.037(13)	4.988(8)	4.947(2)	4.952(3)	4.925(2)	4.930(4)	4.916(2)	4.921(5)
$c/a\sqrt{2}$	1.0194(2)	0.999(4)	1.004(2)		1.002		1.000		1.000
Zr^{4+} ion position									
x	1/4	1/4	1/4	0	1/4	0	1/4	0	1/4
y	3/4	3/4	3/4	0	3/4	0	3/4	0	3/4
z	1/4	1/4	1/4	0	1/4	0	1/4	0	1/4
B_{iso}	1.33(1)	3.51(2)	3.25(5)	3.1(2)	3.1(2)	3.1(2)	3.2(3)	3.3(2)	3.4(2)
O^{2-} ion position									
x	1/4	1/4	1/4	1/4	1/4	1/4	1/4	1/4	1/4
y	1/4	1/4	1/4	1/4	1/4	1/4	1/4	1/4	1/4
z	0.057(2)	0.069(5)	0.055(4)	1/4	0.057(10)	1/4	0.022(26)	1/4	0.019(39)
B_{iso}	1.66(1)	3.91(2)	4.5(4)	5.6(2)	5.8(2)	5.7(1)	6.5(9)	8.2(4)	10.0(9)
R_{bragg}	5.36	5.65	3.27	3.94	3.45	4.29	5.32	3.71	5.35
χ^2	0.086	0.110	0.101	0.319	0.219	0.461	0.368	0.335	0.425

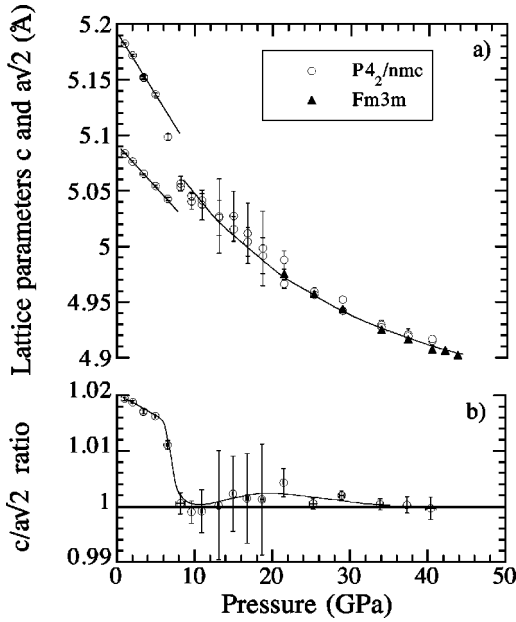


FIG. 4. Lattice parameters c and $a\sqrt{2}$ (a) and anisotropic ratio $c/a\sqrt{2}$ (b) dependence with pressure.

bilized doped zirconia²⁷ in which the authors suggested a linear-quadratic coupling given by the expression $c/a - 1 = 9.08\delta^2$ where c/a measure the structural strain and δ is the order parameter defined as the oxygen shift from the ideal cubic position (see \ddagger in Ref. 27).

Beyond 30 GPa it becomes difficult to choose between the tetragonal and the cubic symmetry without considering carefully the reliability factors. The refinement have been systematically carried out in the $Fm3m$ and $P4_2/nmc$ space groups. Actually the R_{Bragg} factor, which is still of same order at 29 GPa, becomes smaller when the data are fitted in the $Fm3m$ structure. It is quite noticeable for 37.3 GPa. Correlatively, the oxygen atoms tend toward the ideal cubic position (δ tend toward zero). The oxygen isotropic Debye-Waller parameter also decreases when the structure is fitted in the cubic structure. Thus all these results lead us to conclude that the best agreement is obtained with the cubic structure and that the compound evolves continuously to-

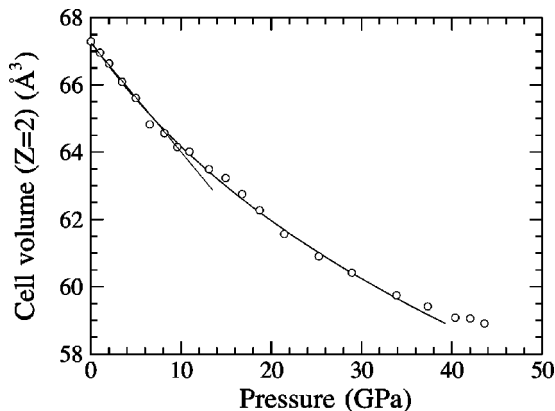


FIG. 5. Cell volume dependence with pressure for the tetragonal and cubic structures. The second-order Birch-Murnaghan equation of state (plain line) defined as follows is also presented: $P = \frac{3}{2}K^0[(V_0/V)^{7/3} - (V_0/V)^{5/3}]\{1 + \frac{3}{4}(K' - 4)[(V_0/V)^{2/3} - 1]\}$.

ward this cubic form as it was concluded from Raman data. The transition pressure is estimated around $P = 30$ GPa.

Furthermore, a high-pressure Raman spectroscopic experiment performed at room temperature on a monoclinic zirconia allowed us to observe the successive monoclinic $\rightarrow O_I \rightarrow O_{II}$ phase transitions, at 7 and 22 GPa, respectively, in agreement with the generalized P - T phase diagram of zirconia given in Ref. 11. Thus comparison between the Raman spectral characteristics of these orthorhombic phases with that of NZ under increasing pressure is another proof that neither the final nor the intermediate state of the compound at high pressure corresponds to any orthorhombic form.

This high-pressure behavior beyond 8 GPa is in good agreement with the conclusion proposed by Wilson, Schönberger, and Finnis from *ab initio* calculation.²⁸ They demonstrate that for a constant $c/a = 1.42$ ($c/a\sqrt{2} = 1.004$) a volume contraction ($\Delta V/V \approx 15\%$) forces the oxygen atoms to move close to their ideal cubic position, because of a progressive disappearance of the double well potential (see Fig. 9 of Ref. 28). In the 8–32-GPa pressure range, the relative volume variation measured in the present work is found equal to 7.5% in qualitative agreement with the above modelization.

Finally, zirconium atoms seem to reach their cubic position at 8 GPa, while the oxygen sublattice has not completely achieved the cubic symmetry. Notice that the data relative to the lattice parameters are mainly based on zirconium positions and are quite reliable. On the opposite, because of the small form factors of oxygen, data based on oxygen positions are much more difficult to obtain. In any case there is no doubt that the structure evolves toward a cubic form, moreover the precise critical pressure cannot be determined with accuracy.

We believe that the observed transition toward a cubic structure is exactly the one which can be expected from the P - T phase diagram of pure zirconia considering that the NZ is equivalent to a pure high-temperature tetragonal zirconia. The size effect is known to induce a strong change in the internal free energy (U) of the compound but does not imply any change neither in the ΔS nor in the ΔV of the tetragonal \rightarrow cubic phase transition. The slope $dP/dT = \Delta S/\Delta V$ of each phase boundary is thus not affected by this size effect. However, translation of the whole phase diagram along T (or P) axes can account for this size effect. The symmetric state observed at 8 GPa cannot be considered as any of the low-temperature orthorhombic state of ZrO_2 (see, for example, recent energy dispersive XRD diffractogram taken by Desgreniers and Lagarec for O_I and O_{II} structures in Ref. 12). Moreover, the elastic anomaly observed at 8 GPa could be discussed considering an interaction between two order parameters driving two different structural changes in zirconium and oxygen sublattices. This discussion is beyond the scope of this paper and will be presented in a forthcoming paper.

B. Determination of structural compressibilities

1. Tetragonal structure

In the low pressure range ($P \leq 8$ GPa) the linear compressibilities along tetragonal crystallographic axes are $\kappa_a = 1.41(5)10^{-12} \text{ Pa}^{-1}$ and $\kappa_c = 2.24(6)10^{-12} \text{ Pa}^{-1}$

TABLE II. Comparison between compressibility (κ) or bulk modulus (K°) measured and calculated for various zirconia. The relationships used to calculate the different compressibilities are $\kappa = 3/(C_{11} + 2C_{12})$ for the cubic structure and $\kappa_a = (C_{33} - C_{13})/[C_{33}(C_{11} + C_{12}) - 2C_{13}^2]$, $\kappa_c = [(C_{11} + C_{12}) - 2C_{13}]/[C_{33}(C_{11} + C_{12}) - 2C_{13}^2]$ and $\kappa = 2\kappa_a + \kappa_c$ for the tetragonal structure. Symbol § corresponds to Birch-Murnaghan second order equation of state. PIB means potential induced breathing model and LDA means local-density approximation.

Fluorite ($Fm\bar{3}m$) $V(Z=4)=143.1$ (\AA^3)	Bulk modulus K° (GPa)	Compressibility $\kappa(10^{-12} \text{ Pa}^{-1})$				
PIB calculation ^a	288	3.46				
10-15-20 wt % Y^{3+} doped ^b	201-203	4.97-4.93				
LDA <i>ab initio</i> calculation ^c	267					
Tetragonal ($P4_2/nmc$) $V(Z=4)=139.4$ (\AA^3)		K°	κ	Linear compressibility		
				κ_a	κ_c	
PIB calculation ^a	173	5.78	1.59	2.59		
12 mol % Ce^{3+} doped ^d						
Neutron diffraction	148	6.76	1.92	2.8		
Lattice-dynamical calculation ^e						
Stabilized zirconia	201	4.97	1.70	1.58		
Pure zirconia	176	5.68	1.92	1.83		
LDA <i>ab initio</i> calculation ^c	200					
This work on undoped NZ						
High-pressure XRD	198(7)	5.06(16)	1.41(5)	2.24(6)		
Equation of state at $P=0.1\text{MPa}$	172(6) [§]	5.8(2) [§]				
	K' 8.5(5)					
Spectroscopic ^f $\kappa_{\Delta\nu}$ B_{1g} 320 cm^{-1}	200(5)	4.9(1)				
Monoclinic ($P2_1/c$) $V(Z=4)=140.6$ (\AA^3)		K°	κ	κ_a	κ_b	κ_c
PIB calculation ^a	185-182	5.4-5.49				
Single crystal ^g						
20<T<1000 °C	201-192	4.97-5.21				
Energy dispersive XRD ^h	212 [§]	4.7 [§]				
Energy dispersive XRD ⁱ	101.1 [§]	9.9 [§]	2.99	2.65	2.43	
LDA <i>ab initio</i> calculation ^c	157	6.4				
Cotunnite ($Pnam$) $V(Z=4)=120.6$ (\AA^3)		K°	κ	κ_a	κ_b	κ_c
High-pressure XRD ^j	332 [§]	3.0 [§]	0.89	0.76	1.04	
LDA <i>ab initio</i> calculation ^c	305	3.3				
Lattice-dynamical calculation ^k	254	3.9				
Energy dispersive XRD ^h	243 [§]	4.1 [§]				

^aSee Ref. 31.

^bSee Refs. 32 and 33.

^cSee Refs. 16 and 18.

^dSee Ref. 34.

^eSee Refs. 35–37.

^fSee Ref. 20.

^gSee Refs. 39 and 40.

^hSee Ref. 12.

ⁱSee Ref. 30.

^jSee Ref. 14.

^kSee Ref. 38.

which confirm that the tetragonal structure is softer along the c axis. The bulk compressibility obtained from the volume cell variation is found equal to $\kappa = 5.2(2)10^{-12} \text{ Pa}^{-1} \approx 2\kappa_a + \kappa_c$. This value satisfies nicely the relationship between bulk and linear compressibilities for a tetragonal sym-

metry.

At $P \approx 8$ GPa, the zirconium sublattice becomes more symmetric and the measured linear and volumic compressibilities are $\kappa_a = \kappa_c = 0.9(1)10^{-12} \text{ Pa}^{-1}$ and $\kappa = 2.7(3)10^{-12} \text{ Pa}^{-1} \approx 3\kappa_a$.

2. Equation of state and spectroscopic compressibilities

Figure 5 presents the pressure dependence of the NZ relative volume at room temperature as obtained from Rietveld refinements of XRD experiment. Initial atomic volume is taken as 67.3 \AA^3 . The second-order Birch-Murnaghan equation of state is also fitted. This state equation considers a linear dependence of the bulk modulus K (defined as the reciprocal of the bulk compressibility) with pressure. Notice that experimental V/V_0 measured beyond 35 GPa were not took into account in the least square optimization of the Birch-Murnaghan equation of state because they lead to low K° (i.e., 153 GPa) and unrealistic $K' = (\partial K / \partial P)_T$ (i.e., 12) values according to Hofmeister²⁹ which has shown that values of K' outside 3.8–8.0 range lead to physically unrealistic potentials. Finally, the NZ bulk modulus is found equal to $K^\circ = 172(6) \text{ GPa}$ with $K' = 8.5(5)$.

Near $P = 0$, these bulk modulus values are slightly different from those determined above. But, referring to literature data, it seems that compressibilities determined from state equation are always slightly overestimated in the low-pressure range. Table II gathers several linear and/or bulk compressibilities measured using high-pressure structural data^{12,14,30} or calculated from the knowledge of the elastic tensor of zirconia polymorphs.^{31–40} Monoclinic and tetragonal structures appear much more compressible than the other polymorphs although large dispersion is observed among literature data. The bulk moduli values which achieve the minimum of the least-square distance between experimental data and Birch-Murnaghan equation of state are strongly dependent upon experimental noise. The monoclinic phase is moreover highly prone to twinning and is difficult to obtain as good single crystal.

Nevertheless, the compressibilities which are extracted from quasiharmonic lattice-dynamical calculations for tetragonal zirconia (see Ref. 37) are in good agreement with the present results. However, they do not reproduce correctly the strong anisotropy observed along a and c axes (see Table II).

Another determination of volumic compressibility can be obtained by starting from the Hazen and Finger⁴¹ empirical relationship

$$\kappa_H = 1.33 \frac{d^3}{Z_c}. \quad (1)$$

Using Zr^{4+} charge and $\langle d_{\text{ZrO}} \rangle = 2.227(6) \text{ \AA}$ for the cation-anion average distance at room temperature and atmospheric pressure, one obtains a polyhedron ZrO_8 compressibility $\kappa_H = 3.67(3) 10^{-12} \text{ Pa}^{-1}$. This value is smaller than that measured above. Introduction of the longest ZrO distance, $d_{\text{ZrO}}^* = 2.400(7) \text{ \AA}$ in the above relationship gives a polyhedron compressibility value of $\kappa_H^* = 4.59(4) 10^{-12} \text{ Pa}^{-1}$ in good agreement with the present results deduced from XRD in the low-pressure range.

Finally, using the same harmonic oscillator model as presented in Ref. 42, it is possible to associate a spectroscopic

compressibility to the frequency variation of specific modes involving polyhedral stretching motions. In the harmonic approximation, a polyhedral compressibility can be derived via the following expression in which n is usually taken equal to 13 for short-range approximation in ionic crystals,

$$\kappa_{\Delta\nu} = \frac{6}{n} \frac{\Delta\nu}{\nu} \frac{1}{\Delta P}. \quad (2)$$

Actually, Raman modes at 600 and 650 cm^{-1} (A_{1g} and B_{1g}), although at high frequency, do not correspond to a ZrO_8 expansion as a whole but rather to out of phase stretching leading to a polyhedron shearing and therefore cannot be used in Eq. (2). On the contrary, from a recent normal mode calculation,⁴³ the 320 cm^{-1} B_{1g} mode is found to strongly involved zirconium sublattice expansion and leads to spectroscopic compressibilities $\kappa_{\Delta\nu} = 4.9(1) 10^{-12} \text{ Pa}^{-1}$ in good agreement with those derived from XRD data (see Table II). Moreover, the slope discontinuity which was detected at 10 GPa from the frequency evolution of the Raman lines (see Ref. 20) gives a spectroscopic compressibility at 10 GPa of $\kappa_{\Delta\nu} = 3.1(2) 10^{-12} \text{ Pa}^{-1}$ again in good agreement with the volumic compressibility measured by XRD at 8 GPa.

Finally, we should mention that the linear compressibilities proposed in Ref. 20, using a linear chain model to describe the dynamic behavior of ZrO_2 , are far from those determined from XRD data, although they reproduced the strong anisotropy observed between compressibilities along a and c axes. In the linear chain model, the force constant between atomic planes are assumed to be linked to microscopic ZrO stretching force constant by simple geometrical relationships. The linear compressibilities were deduced from the variation of these stretching force constants with pressure, using the force constant/bond length dependence given by Michel, Van Den Borre, and Ennaciri.⁴⁴ The poor agreement is probably due to the fact that this law is not valid particularly at short interatomic distances.

V. CONCLUSION

High pressure x-ray diffraction performed on undoped tetragonal zirconia stabilized at room temperature via size effect demonstrates that this compound evolves continuously toward a fluorine structure as it was suspected from Raman spectrometry measurements. The zirconium atoms seems to achieve this cubic structure as soon as 8 GPa and one must reach pressure above 30 GPa to force the oxygen atoms to achieve the ordered fluorine structure. Linear compressibilities an bulk modulus of the tetragonal structure have been measured at atmospheric pressure and ambient temperature. They are found equal to $\kappa_a = 1.41$ and $\kappa_c = 2.24 10^{-12} \text{ Pa}^{-1}$ and $K = 198 \text{ GPa}$. These values are in good agreement with those which can be estimated from vibrational data provided appropriate phonons can be identified.

*Author to whom correspondence should be addressed. Email address: Pierre.Bouvier@lepmi.inpg.fr

†Email address: Guy.Lucazeau@lepmi.inpg.fr

¹D.K. Smith and C.F. Cline, J. Am. Ceram. Soc. **45**, 249 (1962).

²G. Teufer, Acta Crystallogr. **15**, 1187 (1962).

³E.D. Whitney, J. Electrochem. Soc. **112**, 91 (1965).

⁴J.D. McCullough and K.N. Trueblood, Acta Crystallogr. **12**, 507 (1959).

- ⁵D.K. Smith and H.W. Newkirk, *Acta Crystallogr.* **18**, 983 (1965).
- ⁶S. Block, J.A.H da Jornada, and G.J. Piermarini, *J. Am. Ceram. Soc.* **68**, 497 (1985).
- ⁷O. Ohtaka, T. Yamanaka, S. Kume, E. Ito, and A. Navrotsky, *J. Am. Ceram. Soc.* **74**, 505 (1991).
- ⁸O. Ohtaka, T. Yamanaka, S. Kume, N. Hara, H. Asano, and F. Izumi, *J. Am. Ceram. Soc.* **78**, 233 (1995).
- ⁹C.J. Howard, E.H. Kisi, and O. Ohtaka, *J. Am. Ceram. Soc.* **74**, 2321 (1991).
- ¹⁰L.G. Liu, *J. Phys. Chem. Solids* **41**, 331 (1980).
- ¹¹J.M. Leger, P.E. Tomaszewski, A. Atouf, and A.S. Pereira, *Phys. Rev. B* **47**, 14 075 (1993).
- ¹²S. Desgreniers and K. Lagarec, *Phys. Rev. B* **59**, 8467 (1999).
- ¹³O. Ohtaka, T. Yamanaka, and T. Yagi, *Phys. Rev. B* **49**, 9295 (1994).
- ¹⁴J. Haines, J.M. Leger, and A. Atouf, *J. Am. Ceram. Soc.* **78**, 445 (1995).
- ¹⁵J. Haines, J.M. Leger, S. Hull, J.P. Petit, A.S. Pereira, C.A. Perottoni, and J.A.H. da Jornada, *J. Am. Ceram. Soc.* **80**, 1910 (1997).
- ¹⁶J.K. Dewhurst and J.E. Lowther, *Phys. Rev. B* **57**, 741 (1998).
- ¹⁷G. Jomard, T. Petit, A. Pasturel, L. Magaud, G. Kresse, and J. Hafner, *Phys. Rev. B* **59**, 4044 (1999).
- ¹⁸J.E. Lowther, J.K. Dewhurst, J.M. Leger, and J. Haines, *Phys. Rev. B* **60**, 14 485 (1999).
- ¹⁹J. Godlewski, P. Bouvier, G. Lucazeau, and L. Fayette, *ASTM Spec. Tech. Publ.* **1354**, 877 (1998).
- ²⁰P. Bouvier and G. Lucazeau, *J. Phys. Chem. Solids* **61**, 569 (2000).
- ²¹E. Djurado and E. Meunier, *J. Solid State Chem.* **141**, 191 (1998).
- ²²E. Djurado, P. Bouvier, and G. Lucazeau, *J. Solid State Chem.* **149**, 399 (2000).
- ²³G.J. Piermarini, S. Block, J.D. Barnett, and R.A. Forman, *J. Appl. Phys.* **46**, 2774 (1975).
- ²⁴J. Rodriguez-Carvajal, *Physica B* **192**, 55 (1993).
- ²⁵H. Olijnyk, *J. Chem. Phys.* **93**, 8968 (1990).
- ²⁶Ph. Gillet, G. Fiquet, I. Daniel, B. Reynard, and M. Hanfland, *Phys. Rev. B* **60**, 14 660 (1999).
- ²⁷C.J. Howard, B.A. Hunter, and D.-J. Kim, *J. Am. Ceram. Soc.* **81**, 241 (1998).
- ²⁸M. Wilson, U. Schönberger, and M.W. Finnis, *Phys. Rev. B* **54**, 9147 (1996).
- ²⁹A.M. Hofmeister, *Geophys. Res. Lett.* **20**, 635 (1993).
- ³⁰S. Kawasaki and T. Yamanada, *J. Mater. Sci. Lett.* **13**, 514 (1994).
- ³¹R.E. Cohen, M.J. Mehl, and L.L. Boyer, *Physica B* **150**, 1 (1988).
- ³²J. Cai, C. Raptis, Y.S. Raptis, and E. Anastassakis, *Phys. Rev. B* **51**, 201 (1995).
- ³³H.M. Kandil, J.D. Greiner, and J.F. Smith, *J. Am. Ceram. Soc.* **67**, 341 (1984).
- ³⁴E.H. Kisi and C.J. Howard, *J. Am. Ceram. Soc.* **81**, 1682 (1998).
- ³⁵A.P. Mirgorodsky, M.B. Smirnov, P.E. Quintard, and T. Merle-Méjean, *Phys. Rev. B* **52**, 9111 (1995).
- ³⁶A.P. Mirgorodsky, M.B. Smirnov, and P.E. Quintard, *Phys. Rev. B* **55**, 19 (1997).
- ³⁷A.P. Mirgorodsky, M.B. Smirnov, and P.E. Quintard, *J. Phys. Chem. Solids* **60**, 985 (1999).
- ³⁸A.P. Mirgorodsky and P.E. Quintard, *J. Am. Ceram. Soc.* **82**, 3121 (1999).
- ³⁹M.V. Nevitt, S.K. Chan, J.Z. Liu, M.H. Grimsditch, and Y. Fang, *Physica B* **150**, 230 (1988).
- ⁴⁰S.K. Chan, Y. Fang, M. Grimsditch, Z. Li, M.V. Nevitt, W.M. Robertson, and E.S. Zouboulis, *J. Am. Ceram. Soc.* **74**, 1742 (1991).
- ⁴¹R.M. Hazen and L.W. Finger, *J. Geophys. Res.* **84**, 6723 (1979).
- ⁴²S. Loridant and G. Lucazeau, *J. Raman Spectrosc.* **30**, 485 (1999).
- ⁴³P. Bouvier, H.C. Gupta, and G. Lucazeau (unpublished).
- ⁴⁴D. Michel, M.T. VanDenBorre, and A. Ennaciri, *Adv. Ceram.* **24**, 555 (1988).